Influence of Aerosol Scattering on the Retrieval of CO_2 Mixing Ratios: A Case Study Using Measurements from the California Laboratory for Atmospheric Remote Sensing (CLARS)

Qiong Zhang[1], Vijay Natraj[2], King-Fai Li[3], Run-Lie Shia[1], Dejian Fu[2], Thomas J. Pongetti[2], Stanley P. Sander[2], and Yuk L. Yung[1]

[1]Division of Geological and Planetary Sciences, California Institute of Technology, Pasadena, CA, USA

[2]Jet Propulsion Laboratory, California Institute of Technology, Pasadena, CA, USA

[3]Department of Applied Mathematics, University of Washington, Seattle, WA, USA

Corresponding author: Qiong Zhang (qzh@caltech.edu)

Abstract

[1] Column abundances of greenhouse gases in the Los Angeles (LA) basin have recently been measured in the near-infrared spectral region using the California Laboratory for Atmospheric Remote Sensing Fourier Transform Spectrometer (CLARS-FTS) deployed at Mt. Wilson, California since August 2011. In the presence of haze, aerosol scattering causes a variable bias in the measured slant column densities (SCDs). We apply an analytic radiative transfer model and a numerical two-stream model to estimate the impact of neglecting aerosol scattering on the CO_2 and O_2 SCDs operationally retrieved from CLARS-FTS measurements. A retrieval scheme has been developed, and tested using synthetic data. The simulations are performed using a set of aerosol optical depths (AODs) that are representative of the meteorological conditions on 23 March 2013, and a viewing geometry that is nearly identical to the CLARS-FTS measurement configuration. These simulations show that the CLARS-FTS operational retrieval algorithm likely underestimates CO_2 abundances in both the planetary boundary layer and the free troposphere over the LA basin in scenes with medium aerosol loading (AOD ~ 0.1, representative of conditions on 23 March 2013). We also discuss the biases in the CLARS-FTS operational products due to neglecting aerosol scattering.

45 **1. Introduction**

46 [2] Measuring concentrations of greenhouse gases (GHGs, see the list of
47 abbreviations and acronyms in Appendix A for reference) is critical to improve our
48 understanding of their impacts on climate change [*IPCC AR5,* 2013]. Megacities,
49 such as Los Angeles (LA), are immense sources of global GHGs. These areas, which
50 contain more than 50% of the world's population, are contributing at least 70% of
51 fossil fuel CO_2 emissions and a large amount of anthropogenic CH_4 [*Duren and*
52 *Miller*, 2012; *Kort et al.*, 2012]. In the past decade, satellite observations such as
53 those from the Scanning Imaging Absorption Spectrometer for Atmospheric
54 Chartography (SCIAMACHY), the Greenhouse gases Observing Satellite (GOSAT)
55 and the Orbiting Carbon Observatory-2 (OCO-2) were used or have been proposed
56 to measure the global distribution of GHGs [*Bovensmann et al.*, 1999; *Butz et al.*,
57 1999; *Crisp et al.*, 2004; *Kuang et al.*, 2002; *Yokota et al.*, 2009]. However,
58 operational trace gas retrieval algorithms for space missions often apply simplified
59 aerosol models to speed up data processing. To mitigate the impacts of imperfect
60 aerosol/cloud modeling, these retrieval algorithms perform target scene screening
61 that filters out those observations where aerosol and cloud optical depths
62 (AOD/COD) exceed a pre-set threshold value. In the near-infrared, an optical depth
63 of 0.3 is a typical threshold value of AOD. Over megacities where aerosols often
64 reside in the urban planetary boundary layer (PBL), the majority of remote sensing
65 measurements from space are usually filtered out by pre- or post-screening [*Crisp et*
66 *al.*, 2012; *Yoshida et al.*, 2011]. Hence, there exists a need to fill in the “gap” of

satellite measurements, e.g., in the source areas that are significantly contributing to the global GHG emissions.

[3] To measure GHG concentrations in LA, the California Laboratory for Atmospheric Remote Sensing Fourier Transform Spectrometer (CLARS-FTS) was deployed on the top of Mt. Wilson, looking down at the land surface of target sites in the LA basin. There are two modes of operation as shown in Figure 1 [*Fu et al.*, 2013, supplementary figure 1]: (1) Los Angeles Basin Surveys (LABS) mode using reflected sunlight from the LA basin that undergoes absorption and scattering by trace gases and aerosols below the CLARS site; (2) Spectralon Viewing Observation (SVO) mode using reflected sunlight from a locally positioned Spectralon plate that samples the solar beam above the CLARS site and measures the background GHG abundances in the free troposphere above Mt. Wilson. CLARS-FTS has high sensitivity to the variation of GHGs over LA basin due to the long light path traveling through the urban PBL (typically 20 km distance from CLARS site to the LA basin land surface). In the LABS mode, sunlight travels through the PBL twice, with a large viewing zenith angle, prior to being measured by the instrument. This viewing geometry offers much higher sensitivity to the atmospheric composition within the PBL than a typical satellite geometry but also makes the measurements more susceptible to the influence of aerosol scattering and absorption. The current CLARS-FTS operational retrieval algorithm (version 1.0) uses measurements of the CO_2 absorption band centered at 1.61 μm to estimate the CO_2 slant column density (SCD) along the line of sight. The SCD is defined as the total number of absorbing

89 gas molecules along the optical path per unit area. The effect of aerosol scattering,
90 on the other hand, can be estimated by simultaneously retrieving the O_2 SCD based
91 on measurements of the O_2 absorption band centered at 1.27 μm, assuming that the
92 changes in light path due to aerosol scattering are identical in both the 1.61 μm and
93 1.27 μm bands. This approach leads to an underestimation of CO_2 and O_2 SCDs due
94 to a "line filling-in" effect (see Section 3) in the absorption lines. The bias due to
95 aerosol scattering can be reduced by estimating the column-averaged dry air mole
96 fraction of CO_2 (X_{CO_2}), defined as 0.2095 (known O_2 volume mixing ratio) times the
97 CO_2 SCD divided by the O_2 SCD. However, the wavelength dependence of aerosol
98 scattering implies that division by O_2 SCD does not completely remove the aerosol
99 scattering effect in the 1.61 μm band. The assumption that aerosol scattering is
100 identical in the two bands leads to an observable bias in the retrieved X_{CO_2}.
101 Therefore, a proper retrieval must account for wavelength-dependent aerosol
102 scattering.

103 [4] Aerosol composition and mass loading in the LA area were studied during
104 previous campaigns such as the California Research at the Nexus of Air Quality and
105 Climate Change (CalNex) [*Hersey et al.*, 2011, 2013] and the Southern California
106 Ozone Study (SCOS) [*Collins et al.*, 2000]. However, their optical properties, such
107 as the single scattering albedo (SSA) and the asymmetry parameter (g), are poorly
108 quantified [*Andrews et al.*, 2006]. Most of the previous studies have focused on the
109 effect of aerosols on the planetary energy budget [*Haywood and Shine*, 1995;
110 *Takemura and Nakajuma*, 1995] instead of providing the optical properties needed

111 for an algorithm to retrieve trace gas abundances. Recently, *Seidel and Popp* [2012]
112 studied the relationship between surface albedo and aerosol SSA and its implications
113 for retrieving AOD using reflected radiance. Similarly, studies on aerosol scattering
114 and absorption were carried out by *Belton et al.* [1968] and *Chamberlain* [1970] for
115 a semi-infinite planetary atmosphere without considering surface reflection.
116 *Houweling et al.* [2005] studied the retrieval bias from SCIAMACHY measurements
117 and confirmed that the large variability in the total column CO_2 retrieved over the
118 Sahara Desert was caused by mineral dust. However, they did not perform detailed
119 modeling to relate the optical properties of mineral dust to the observed radiance to
120 explain the variability in retrieved total column CO_2.

121 [5] One possible explanation for the retrieval bias caused by aerosols is related
122 to the photon path length distribution. *Oshchepkov et al.* [2012] studied the effect of
123 aerosols on optical path variations for reflected sunlight observed from space and
124 developed a method to filter out data highly contaminated by aerosols and clouds. In
125 a study by *Funk and Pfeilsticker* [2003], the photon path length distribution was used
126 to study radiative transfer in clouds. Since this method is based on statistical results,
127 it is difficult to quantify the relationship between gaseous absorption and aerosol
128 scattering.

129 [6] Our aim is to understand the influence of aerosol scattering on the observed
130 radiance using fundamental principles of radiative transfer. In Section 2, we first
131 demonstrate the retrieval bias in CO_2 and O_2 SCD due to neglecting aerosol
132 scattering, which manifests itself as a ‘U-shape’ in a plot of the retrieved SCD

against the geometric SCD. In Section 3, we present an analytic two-stream radiative transfer model [*James*, 1975; *Liou*, 1974; *Meador and Weaver*, 1979], employing Lorentzian absorption line shapes for O_2 and CO_2, to show the spectral signatures of aerosol scattering on the observed radiance. In Section 4, both the analytic model and the numerical two-stream model are used to illustrate how aerosol scattering causes an apparent reduction in the retrieved abundances of trace gases as manifested by the 'U shape'. The retrieval biases in the PBL and the free troposphere are evaluated under different scenarios. Section 5 presents the conclusions and discusses the implications of this work.

2. Underestimation of SCDs due to aerosol scattering

[7] Here we will demonstrate the SCD retrieval bias due to the assumption of neglecting aerosol scattering. Although we perform our analysis on the CLARS-FTS measurements, the results are generally applicable to similar ground-based and space-based measurements.

[8] In the LABS mode, CLARS-FTS points at a programmed sequence of ground target locations in the LA basin. Sample CO_2 SCDs along the line of sight from the CLARS site on Mt. Wilson to a target in West Pasadena retrieved during a hazy day are shown in Figure 2(a). For scenarios over the LA basin with medium aerosol loading (AOD ~ 0.1), we obtain a 'U shape' as the SCD of absorbing gas along the line of sight changes from the morning to the afternoon. The data are closer to the 1:1 line in the morning (A-B) and deviate from it as the haze builds up

155 in the afternoon (B-C). For a pure trace gas absorption scenario, i.e. with no aerosol
156 scattering in the atmosphere, we expect the measured SCD to agree with the
157 calculated geometric SCD. Therefore the data points, such as those in the SVO mode
158 measurements (green "+" points in Figure 2) must fall on the 1:1 line. For the
159 measurements over West Pasadena, the observed CO_2 SCDs are systematically
160 smaller (by up to 13%) than the geometric ones from the morning to the afternoon.
161 Figure 2(b) shows similar deviation (by up to 17%) in the O_2 SCD. The deviation of
162 CO_2 could arise from diurnal variations (i.e., changes of CO_2 emission rate over the
163 LA basin, etc). However, there are no emission sources in the LA basin for O_2. This
164 suggests that the low bias is due mainly to the increase in AOD during the daytime,
165 as indicated by the images recorded by a visible camera that was co-aligned with the
166 CLARS-FTS. The current CLARS retrieval algorithm uses the GFIT model [*Fu et al*,
167 2013], which does not include aerosol scattering. Since aerosol scattering has
168 wavelength dependence, we expect the O_2 and CO_2 SCD to have different deviations
169 from the 1:1 line. Normalizing the CO_2 SCD by the O_2 SCD cannot completely
170 eliminate the biases in X_{CO_2} caused by aerosol scattering.
171
172 **3. Influence of aerosols on the observed radiance**
173 [9] Using a sophisticated numerical two-stream Radiative Transfer Model (RTM)
174 [*Spurr and Natraj*, 2011], where the radiative transfer calculation is done
175 analytically except for the boundary value problem (which is also done using a
176 simple and fast pentadiagonal solver rather than typical matrix inversion techniques),

177 we simulate spectra using configurations similar to the CLARS-FTS measurements.
178 Figure 3 shows synthetic spectra in the 1.27 μm O_2 absorption band with different
179 AODs in the PBL. The spectra from the two-stream RTM have been validated
180 against a full-physics RTM model VLIDORT [*Spurr*, 2006], which provides
181 radiances with an accuracy higher than the two-stream RTM. There are two
182 prominent features. First, the spectral continuum level increases with AOD (Figure
183 3(a)). Second, after normalizing the radiance by its maximum value, the absorption
184 lines move upward in the regions of weak absorption, hereafter referred to as "line
185 filling-in". The full width at half maximum (FWHM) of the spectral lines in Figure
186 3(b) shows that the absorption becomes weaker as AOD increases. This line
187 filling-in is a consequence of radiance normalization. In Figure 3(c), the synthetic
188 spectra and real measurements from CLARS-FTS on 13 March 2013 (clear) and 23
189 March 2013 (hazy) are shown. The measurements are made at nearly identical local
190 times (4:30 pm) but on two days not far apart to obtain nearly identical solar zenith
191 angles (SZAs). AOD is estimated based on images from a co-boresighted visible
192 camera. The spectral lines measured on a hazy day (red line in Figure 3(c)) move
193 inward and show weaker absorptions, compared with the ones recorded on a clear
194 day (blue line in Figure 3(c)). This line filling-in is observed in both the
195 CLARS-FTS measured spectra (Figure 3(c)) and the simulations (Figure 3(b)).
196 Similarly, the line filling-in is apparent in spectra of the CO_2 absorption bands.

197 [10] The spectral features can be explained by a simple analytic model as
198 described in Appendix B. First, to simplify the problem and show the influence of

aerosol on the magnitude of the reflected radiance, we derive the reflectance, R, of a single-layer atmosphere with aerosol absorption and scattering only (Appendix B.1). In this model, the incoming solar flux is absorbed by both the atmosphere and the surface, and reflected by the PBL. Simple derivations show that (equation (B15)) R is a monotonic function with respect to AOD in the PBL, τ_1, depending on the value of the SSA, ω_0. If ω_0 is high compared to the surface albedo, α, as is the case for sulfate and sea-salt aerosols, R increases with τ_1. However, if ω_0 is low, as is the case for black carbon, R decreases with τ_1.

[11] Of interest, then, is the transition point at which the derivative of R with respect to τ_1 changes sign. We assume that the surface albedo is fixed for most scenarios; however, the SSA of aerosols in the atmosphere may vary widely. The critical SSA, ω_c, is defined as the SSA at which increasing AOD does not change the magnitude of the reflected radiance (equal to the scene without aerosol). Mathematically we can derive it as follows.

$$\lim_{\tau_1 -> \infty} R(\tau_1, \omega_c) = \frac{[\omega_c - \alpha(1-\bar{\mu}\rho)^2]}{[(1+\bar{\mu}\rho)^2 - \alpha\omega_c]} = \alpha \quad (1)$$

$$\omega_c = \frac{4\alpha}{(1+\alpha)^2} \quad (2)$$

The values of ρ and $\bar{\mu}$ are defined in Appendix B1. In equation (2), ω_c is a simple monotonic function of just the surface albedo. This relationship still holds in an atmosphere with both aerosol scattering and gaseous absorption. When the surface albedo is low, the aerosol SSA must be much larger than the surface albedo in order to increase the observed radiance by scattering at the top of the PBL. To confirm this

220 relationship and to test our analytic solution, we compare our results with the results
221 of *Seidel and Popp* [2012], in which they perturb the AOD in a numerical model for
222 different scenarios to get the value of the critical SSA. An important implication of
223 this relationship is that if the SSA of aerosols in the PBL approaches ω_c, it is difficult
224 to retrieve the AOD even if the instrument is well calibrated. In this scenario,
225 sensitivity of the reflected radiance to the aerosol parameters will decrease and
226 retrieval errors will increase.

227 [12] To explain the line filling-in, we use a one-line absorption model for CO_2
228 and O_2 (Appendix B.2). Taking CO_2 as an example, Figure 4 shows the calculated
229 reflectance. In this case, the absorption line becomes weaker after normalization (by
230 the maximum value of the radiance) as shown in Figure 4(b) for $\omega_0 = 0.99$, larger
231 than the critical value corresponding to the surface albedo of 0.1. This suggests that
232 the gaseous absorption is reduced by aerosol scattering. This effect can be intuitively
233 understood as follows: before the sunlight reaches the surface, it is scattered to the
234 point of observation at the top of the PBL without going through the atmosphere
235 below, thereby reducing the absorption optical path in the PBL. This effect is
236 independent of aerosol type. We also calculate the reflectance with $\omega_0 = 0.2$, less
237 than the critical value, as shown in Figures 4(a) and 4(c). The reflectance decreases
238 with AOD, but after normalization, we can still see the line filling-in. In Figure 4(d),
239 we obtain similar line filling-in effects by reducing the concentration of CO_2 in the
240 calculation and setting AOD in the PBL to zero. For an O_2 absorption line centered
241 at $\nu_0 = 7863.4$ cm^{-1}, all the features are similar (not shown here).

[13] Using normalized spectra, the equivalent effects of absorption line filling-in caused either by reducing absorbing gas concentration or by aerosol scattering in the PBL are difficult to distinguish. In a model without aerosol scattering, all the changes in line width are attributed to changes in gas abundance. This explains the changes in retrieved SCDs from CLARS-FTS as AOD increases from the morning to the afternoon (Figure 2).

4. Retrieval bias caused by aerosol scattering

[14] In order to quantify the influence of aerosol scattering on GHG retrieval and simulate the bias observed by CLARS-FTS, we employ the Levenberg-Marquardt (LM) algorithm [*Rodgers*, 2000] to retrieve CO_2 and O_2 concentrations. The iteration in the retrieval algorithm is:

$$x_{i+1} = x_i + [(1+\gamma)\mathbf{S}_a^{-1} + \mathbf{K}_i^T \mathbf{S}_e^{-1} \mathbf{K}_i]^{-1} \{\mathbf{K}_i^T \mathbf{S}_e^{-1} [y - \mathbf{F}(x_i)] - \mathbf{S}_a^{-1} [x_i - x_a]\} \quad (3)$$

where x is the retrieved state vector, x_a is the *a priori* state vector, y is the measured spectral radiance, S_a is the *a priori* covariance matrix, S_e is the spectral radiance noise covariance matrix, K is the Jacobian matrix, F(x) is the forward model and γ is the parameter determining the size of each iteration step. The number of degrees of freedom (DOF) measures how many independent pieces of information we can obtain from the measurement. It can be calculated as:

$$DOF = \sum_i \lambda_i^2 / (1+\lambda_i^2) \quad (4)$$

where $\{\lambda_i\}$ are the singular values of the Jacobian, K.

[15] Both the analytic and numerical models are employed in this work. We

assume nonzero AOD evenly distributed in the PBL to generate synthetic data. However, in the retrieval, the AOD is set to zero and held constant. This approach approximately simulates the influence of neglecting aerosol scattering on the retrieved values of SCD. The model configurations used in this section are listed in Table 1.

4.1 Analytic model

[16] Using the analytic model described in Appendix B (case A in Table 1), we choose a spectral window of 2 cm^{-1} around the central wavenumber of ν_0 = 6243.9 cm^{-1} for CO_2 and ν_0 = 7863.4 cm^{-1} for O_2. The sampling interval is 0.001 cm^{-1}; therefore, 2000 channels are used. Synthetic data are generated using normalized spectra for a signal-to-noise ratio (SNR) of 300, similar to that of a CLARS-FTS measured spectrum. The model sampling interval (spectral point spacing) is much smaller than the CLARS-FTS sampling interval; however, it provides a DOF close to 2 for both CO_2 and O_2 with only one absorption line, thereby enabling us to retrieve trace gas abundances in the PBL and the free troposphere simultaneously. In the retrieval algorithm, the *a priori* and the first guess of CO_2 concentrations in the two layers are set at 400 ppm, which are different from the true values of 410 ppm in the PBL and 390 ppm in the free troposphere. For the O_2 concentration, the *a priori* and the true values in both the layers are set at 0.2095.

[17] Figure 5 shows retrieved CO_2 concentrations in both the PBL and the free troposphere with increasing AOD. It is worthwhile to note that this is performed prior to normalizing the CO_2 column by the O_2 columns, i.e., completely neglecting the

impacts of aerosol scattering on light path computations. When the AOD is identical to zero, we can retrieve the true values of CO_2 concentrations in both layers, showing that our retrieval algorithm is robust. Since the AOD decreases from the surface to higher altitudes, the bias in the PBL (solid line) is much larger than that in the free troposphere (dashed line). The analytic model requires identical slant path optical depths in the incoming and outgoing directions. Therefore, the model requires the viewing zenith angle always to match the SZA. In the LABS mode measurements, the viewing zenith angles are larger than the SZA (greater than 60^o). When the SZA and the viewing angle are increased from 0^o to 60^o, the CO_2 concentration differences between the retrieved and true states also increase (Figure 5). This shows that both AOD and SZA are important factors affecting the retrieval of absorbing gas concentrations.

[18] In Figure 6, we retrieve the CO_2 and O_2 SCDs assuming the SZA varies linearly from 60° to 0° and back to 60° with the AOD increasing linearly from 0 to 0.1 in the PBL. It shows approximately one day of simulated measurements from the morning to the afternoon (8:00 am to 4:00 pm). The SCD is defined in equation (5), where P_s is the surface pressure, P_1 is the pressure at the top of PBL, χ_1 is the absorbing gas concentration in the PBL, χ_2 is the absorbing gas concentration in the free troposphere, $M = 2.067\times10^{22}$ molecule cm^{-2} hPa^{-1} is the total number of air molecules per unit area per unit pressure. Our model is approximate in many ways. Therefore, if we compare Figure 6 with the measurements in Figure 2, we can expect only qualitative agreement.

$$SCD = \frac{2\chi_1(P_s - P_1) + \chi_2 P_1}{\cos(SZA)} M \quad (5)$$

[19] As the AOD increases, the retrieved SCD falls off the 1:1 line of geometric SCD, similar to the daily trend of SCD measured by the CLARS-FTS on 23 March 2013 over West Pasadena. The CLARS-FTS operational retrieval algorithm uses the O_2 SCD to normalize the CO_2 SCD. This method can eliminate the uncertainties in light path computation to first order. However, some errors persist because the aerosol scattering depends on wavelength. In addition, because the spectroscopic parameters such as line strength and pressure broadening coefficients for O_2 and CO_2 are different, the two biases are likely not identical. When the aerosol SSA is decreased to 0.2, the retrieval also underestimates the true SCD, consistent with the analysis in section 3 on spectral line filling-in for low SSA scenarios. However, the biases are much smaller compared with the cases with higher SSA because for a given AOD, the filling in is less significant (see Figure 4c).

4.2 Numerical model

[20] The analytic model provides an explanation for the retrieval bias caused by aerosol scattering. However, there are several approximations in this first-order analytic model. The incoming solar flux is approximated by an isotropic diffusive flux at the top of the model. In the PBL, the viewing zenith angle and SZA must be identical in order to ensure the same slant path optical depths for the incoming and outgoing beams. These assumptions may cause the model to deviate from the measurements. In order to better simulate CLARS-FTS measurements, and to explore

330 the effects of aerosol scattering in a more realistic parameter space, we use a
331 numerical two-stream RTM [*Spurr and Natraj*, 2011] to simulate the observed spectra
332 in a spectral interval broader than those in Figures 3 – 4. The CO_2 and O_2 spectral
333 ranges shown in Figure 7 are based on *Fu et al.* [2013] and each covers 25 cm^{-1} (the
334 CLARS-FTS operational algorithm used spectral regions wider than 25 cm^{-1}). In this
335 model, the *a priori* atmospheric profile has 70 layers from the surface up to 70 km and
336 is derived from NCEP-NCAR reanalysis data [*Kalnay et al.*, 1996]. We calculate the
337 optical depth for each layer using the Reference Forward Model [*Dudhia et al.*, 2002],
338 and then simulate the reflected radiance observed by the CLARS-FTS. We assume the
339 surface reflection to be Lambertian with a surface albedo of 0.23, as measured for
340 West Pasadena [*Fu et al.*, 2013]. The model takes into consideration Rayleigh
341 scattering by air molecules. The viewing zenith angle, a constant parameter, is 83.1^{o}
342 for the target scene over West Pasadena. SZAs at a given date can be calculated as
343 shown in equations (6)-(7):

344 $$\cos(SZA) = \cos(L)\cos(\delta)\cos(H) + \sin(L)\sin(\delta) \quad (6)$$

345 $$H = \frac{(\text{minutes past midnight}) - 720}{4\,\text{min/ deg}} \quad (7)$$

346 where L is the latitude (34.2^{o} for West Pasadena) and δ is the declination angle (0.2^{o}
347 for 23 March 2013). H is the hour angle measuring the time difference from the local
348 noon.

349 [21] In the forward model, we apply the CLARS-FTS instrument line shape (ILS)
350 with FWHM = 0.22 cm^{-1} [*Fu et al.*, 2013] to the simulated radiances and Jacobian
351 matrices for absorbing gas concentrations. The sampling interval is 0.06 cm^{-1}, and the

SNR is 300. To investigate the impacts of aerosol scattering on the SCD of CO_2 and O_2, the algorithm retrieves the two species separately. For each species, two scaling factors are retrieved, one for the mean gas concentration in the PBL and the other for the free tropospheric concentration.

[22] We selected a target scene with a SZA of 54.1^o to study the retrieval bias as a function of AOD. Figure 8 shows the influence of aerosol scattering on the retrieved concentrations of CO_2 and O_2. We assume an idealized aerosol with SSA = 0.99 and asymmetry parameter g = 0 (case B in Table 1). For CO_2, the true values of the concentration scale factors in the PBL and the free troposphere are set to 1.1 and 0.9 respectively, which are different from the *a priori* vertical profile. Without the influence of aerosols, we retrieve the true values as shown in Figure 8(a). The features shown here for the decrease in concentration with increasing AOD are similar to the analytic model (Section 4.1, Figure 5). The retrieval bias in the PBL is much larger than that in the free troposphere. It is worthwhile to note that the bias in the O_2 retrieval is slightly larger than that in the CO_2 retrieval, due to the wavelength dependence of aerosol scattering. Figure 8(c) shows X_{CO_2} as a function of AOD. The sign of this bias is dependent on the AOD. An algorithm that calculates X_{CO_2} (equation (8)), i.e., the approach used in the CLARS-FTS operation algorithm, can greatly reduce the bias due to aerosol scattering. However, the scaling factor of X_{CO_2} shown in Figure 8(c) still deviates from the true value. The biases between retrieved X_{CO_2} and the true values are up to 3%, because this approach (equation (8)) neglects

wavelength dependence of aerosol scattering between the CO_2 and O_2 absorption bands.

$$X_{CO_2} = 0.2095 \frac{SCD_{CO_2}}{SCD_{O_2}} \quad (8)$$

[23] For non-isotropic aerosol scattering, we explore the retrieval bias in the SSA-g parameter space (case C in Table 1) as shown in Figure 9. We assume that the aerosol scattering has a Henyey-Greenstein type phase function [*Boucher*, 1998; *Henyey and Greenstein*, 1941] with SSA ω_0 and asymmetry parameter g. The AOD is kept constant at 0.1. We find that the retrieved SCD is always less than the geometric SCD calculated from the true atmospheric profile. This is because aerosol scattering causes absorption line filling-in, as described in Section 3. When calculating X_{CO_2} using equation (8) without taking the wavelength dependence into account, the mean mixing ratio could be either over- or under-estimated, depending on the relative magnitude of biases in the CO_2 and O_2 SCDs. The bias in X_{CO_2} is much smaller than that in the CO_2 SCD. This indicates that dividing the CO_2 SCD by that of O_2 removes some of the biases due to aerosol scattering. However, the wavelength dependence of aerosol scattering still causes biases in X_{CO_2}, the magnitude of which is dependent on the AOD. At constant AOD, the biases in both X_{CO_2} and SCDs are dependent on both SSA and g. The retrieval bias of SCD increases with SSA, consistent with Figure 6, and decreases with g. The latter can be intuitively understood as follows: for smaller g, the scattering phase function is more isotropic (less forward peaked). By using the delta-Eddington approximation [*Hansen and Travis*, 1974; *Kylling et al*, 1995; *Wiscombe*, 1977], we can get the equivalent isotropic AOD $\tau_s^{'}$ and

395 SSA ω' for the forward peaked scattering as shown in equations (9)-(10) [*Goody and*

396 *Yung*, 1999; *Liou*, 2002]:

397 $$\tau_s' = (1-f)\tau_s \quad (9)$$

398 $$\omega' = \frac{1-f}{1-f\omega}\omega \quad (10)$$

399 where f is the fraction of scattered energy residing in the forward peak. Therefore a

400 more forward-peaked phase function with large g value will lead to smaller aerosol

401 scattering as well as smaller retrieval bias.

402 [24] To simulate the observed 'U shape' and match the CLARS-FTS retrieved

403 SCD as shown in Figure 2, AOD data are taken from measurements from the AErosol

404 RObotic NETwork (AERONET) station at Caltech on 23 March 2013 [*Holben et al.*,

405 1998; *Holben et al.*, 2001]. AERONET measurements cover the wavelength range

406 from 340 to 1020 nm. However, neither the CO_2 nor O_2 near-infrared band used in our

407 retrievals is included in the AERONET measurements. To calculate the AOD in these

408 two bands, we use the Angstrom exponent law to extrapolate the data [*Seinfeld and*

409 *Pandis*, 2006]

410 $$\frac{\tau}{\tau_0} = \left(\frac{\lambda}{\lambda_0}\right)^{-\kappa} \quad (11)$$

411 where λ_0 and τ_0 are the reference wavelength and the corresponding AOD, and $\kappa = 0.78$

412 is the Angstrom coefficient. The AOD in the CO_2 band starting at 1607 nm is 0.0708,

413 while the AOD in the O_2 band starting at 1264 nm is 0.0854.

414 [25] Aerosol properties in the LA basin were obtained from simulations using the

415 Weather Research and Forecasting [WRF; *Skamarock et al.*, 2005] model. The Modal

Aerosol Dynamics Model/Secondary Organic Aerosol Module (MADE/SORGAM) [*Ackermann et al.*, 1998; *Schell et al.*, 2001] was used to obtain specific values for 5 aerosol types (black carbon, organic carbon, sulfate, coarse and accumulation mode sea salt). The aerosol single scattering properties were computed using the Meerhoff Mie code [*de Rooij and van der Stap*, 1984], with size distribution parameters taken from the Optical Properties of Clouds and Aerosols [OPAC; *Hess et al.*, 1998] database. Table 2 shows the typical aerosol compositions (measured by optical depth) and optical parameters in this region. In the forward model (case D in Table 1), we vary the hour angle H in equation (7) from -75^o to 75^o to simulate different measurements from the morning to the afternoon (7:00 am to 5:00 pm). We assume that the total AOD increases from zero to the value extrapolated from the AERONET station measurements. The temporal variation of AOD is simulated by an idealized function as shown in equation (12).

$$\tau_s = \frac{AOD}{2} + \frac{AOD}{2}\tanh(\frac{H}{30^o}) \quad (12)$$

[26] The simulated variations of CO_2 and O_2 SCD (Figure 10) match the data. Furthermore, the 'U shape' of O_2 SCD also shows larger low bias than CO_2 SCD for the same AOD conditions. This demonstrates that aerosol scattering is the cause of the low bias in the CO_2 and O_2 SCD.

5. Discussion and conclusion

[27] The effects of aerosol scattering on GHG retrievals are analyzed. Analytic solutions provide clear insights into the physical mechanism of aerosol scattering,

438 while the more complex numerical models are more realistic and match the data more
439 accurately. We conclude that in an environment with aerosols, the effect of aerosol
440 scattering is equivalent to a decrease in absorption line width. When using normalized
441 radiances in the retrieval, the retrieved gas abundances show a low bias regardless of
442 the value of aerosol SSA. The observed 'U shape' is simulated with both analytic and
443 numerical models. We compute the SCD retrieval bias in an SSA-g parameter space to
444 analyze the influence of different kinds of aerosols; the results reinforce the
445 conclusion that the retrieved SCD always shows a low bias when using normalized
446 radiance. This result is different from that reported by *Houweling et al.* [2005], who
447 concluded that aerosols over a bright reflective surface will on average extend the
448 light path length. The difference is mainly due to the non-normalized reflected
449 radiance used in their study. As shown in Appendix B.1, if we use the non-normalized
450 radiance instead, aerosols, to first order will cause a decrease in the magnitude of the
451 radiance. To fit the decreased radiance, retrieved gas abundances will show a high
452 bias. This has been tested using our analytic model. An examination of CLARS-FTS
453 measurements on other days confirms that all retrievals of CO_2 and O_2 SCD show low
454 biases without exception.

455 [28] This study has implications for current and future missions measuring GHG
456 abundances such as GOSAT and OCO-2. For these instruments, many measurements
457 with aerosol or cloud contaminations are rejected. With high enough spectral
458 resolution and wide enough spectral range, as in the case of OCO-2, there is great
459 potential to retrieve the GHG vertical profile. Our results (Figure 5 and Figure 8)

460 show that, for a profile retrieval, the bias in the free troposphere is very small, even if
461 we use a RTM that does not include aerosol scattering, such as the GFIT model.
462 Therefore it is possible that many of the rejected measurements could be reanalyzed to
463 yield useful results. Since megacities are important areas of GHG sources, a better
464 remote sensing technique will greatly improve our estimation of the global GHG
465 budget.

466 [29] As a fast approach to correct the X_{CO_2} retrieval bias, we can develop a
467 look up table that stores scaling factors as a function of AOD, such as shown in
468 Figure 8(c). It is also possible to retrieve aerosol properties simultaneously with GHG
469 abundances, thereby eliminating the bias caused by aerosol scattering. However,
470 current full-physics radiative transfer models with aerosol scattering are not fast
471 enough to be used operationally for processing data on a large scale. With a
472 full-physics model, we can calculate the radiance more accurately and match the real
473 measurements. It is also possible to account for the state of polarization to gain extra
474 DOFs and improve the retrieval quality.

475 [30] Furthermore, the simulated retrievals uncover the degeneracy between SSA
476 and surface albedo Jacobians, making the determination of these parameters more
477 difficult. There are several possible solutions. First, calibrating the instrument to
478 obtain absolute radiance can increase the DOF by approximately 1 and the
479 information content by several bits. Second, in principle, the surface albedo can be
480 assumed to be constant for most of the target scenes, thereby mitigating the
481 degeneracy issue. In this work, when using normalized radiance, the bias always tends

to underestimate the retrieved GHG abundances in all scenes with different types/amounts of aerosols. Our preliminary study shows that, even if some aerosol parameters are not accurately retrieved, the retrieval biases for gas abundances can still be greatly mitigated when aerosol parameters are incorporated into the retrieval algorithm. By using more accurate *a priori* aerosol information, such as measurements from the Multiangle Imaging Spectro Radiometer (MISR) and AERONET [*Kahn et al.*, 2005], the retrieval biases can be further reduced. These issues will be the topics of subsequent papers.

Acknowledgements

[31] We thank C. Wong, J. Margolis, S. Newman, C. Miller, D. Crisp, M. Gerstell, X. Xi, P. Kopparla, P. Gao, R. Hu and L. Kuai for helpful comments. This research was supported in part by NASA grant NNX13AK34G to the California Institute of Technology, grant P1367828 from the Jet Propulsion Laboratory and and the KISS program of Caltech.

Appendix A: Abbreviations and acronyms

AERONET	Aerosol Robotic Network
AOD	Aerosol Optical Depth
CalNex	California Research at the Nexus of Air Quality and Climate Change
CLARS	California Laboratory for Atmospheric Remote Sensing
COD	Cloud Optical Depth
DOF	Degree of Freedom
FTS	Fourier Transform Spectrometer
FWHM	Full Width at Half Maximum
g	Asymmetry Parameter
GHG	Greenhouse Gas
GOSAT	Greenhouse Gases Observing Satellite
ILS	Instrument Line Shape
LA	Los Angeles
LABS	Los Angeles Basin Surveys
LM	Levenberg-Marquardt
MADE	Modal Aerosol Dynamics Model
MISR	Multiangle Imaging Spectro Radiometer
OCO-2	Orbiting Carbon Observatory-2

PBL	Planetary Boundary Layer
RTM	Radiative Transfer Model
SCD	Slant Column Density
SCIAMACHY	Scanning Imaging Absorption Spectrometer for Atmospheric Chartography
SCOS	Southern California Ozone Study
SNR	Signal-to-Noise Ratio
SORGAM	Secondary Organic Aerosol Module
SSA	Single Scattering Albedo
SVO	Spectralon Viewing Observation
SZA	Solar Zenith Angle
X_{CO_2}	Column-Averaged Dry Air Mole Fraction of CO_2

Appendix B: Two-stream analytic model

1. Influence of aerosols on radiance

[32] We solve a simplified radiative transfer equation without the source term as shown in equation (B1) to explain the change of radiance due to aerosols [*Goody and Yung*, 1989; *Liou*, 2002]. We assume that the scattering is isotropic and the single scattering albedo ω_0 is a constant. In this equation I is the radiance, τ is the optical depth and $\mu=1/\cos(\theta)$, where θ is the viewing zenith angle or the SZA. This approximation is accurate only to the first order. We neglect the term associated with the incoming solar irradiance and assume that it is the same as the isotropic diffusive flux at the top of the atmosphere.

$$\mu\frac{\partial I(\tau,\mu)}{\partial\tau}=I(\tau,\mu)-\frac{1}{2}\omega_0\int_{-1}^{1}I(\tau,\mu)d\mu \tag{B1}$$

Separating upward and downward streams using two-stream approximation as

$$\bar{\mu}\frac{dI^{+}(\tau,\bar{\mu})}{d\tau}=I^{+}(\tau,\bar{\mu})-\frac{1}{2}\omega_0[I^{+}(\tau,\bar{\mu})+I^{-}(\tau,-\bar{\mu})] \tag{B2}$$

$$-\bar{\mu}\frac{dI^{-}(\tau,-\bar{\mu})}{d\tau}=I^{-}(\tau,-\bar{\mu})-\frac{1}{2}\omega_0[I^{+}(\tau,\bar{\mu})+I^{-}(\tau,-\bar{\mu})] \tag{B3}$$

we can solve for general solutions as below, where $I^{+}(\tau)=I^{+}(\tau,\bar{\mu})$, $I^{-}(\tau)=I^{-}(\tau,\bar{\mu})$.

$$I^{+}(\tau)=(1-\bar{\mu}\rho)c_1e^{-\rho\tau}+(1+\bar{\mu}\rho)c_2e^{\rho\tau} \tag{B4}$$

$$I^{-}(\tau)=(1+\bar{\mu}\rho)c_1e^{-\rho\tau}+(1-\bar{\mu}\rho)c_2e^{\rho\tau} \tag{B5}$$

$$\rho^2=\frac{1-\omega_0}{\bar{\mu}^2} \tag{B6}$$

$$\bar{\mu} = \frac{1}{\sqrt{3}} \tag{B7}$$

Applying the boundary conditions to account for the reflection at the surface, where α is the surface albedo and F is the incoming solar flux, we can get the two-stream general solution with surface albedo at arbitrary optical depth

$$(1+\bar{\mu}\rho)c_1 + (1-\bar{\mu}\rho)c_2 = \frac{1}{2\pi}F \tag{B8}$$

$$(1-\bar{\mu}\rho)c_1 e^{-\rho\tau_1} + (1+\bar{\mu}\lambda)c_2 e^{\rho\tau_1} = \alpha[(1+\bar{\mu}\rho)c_1 e^{-\rho\tau_1} + (1-\bar{\mu}\rho)c_2 e^{\rho\tau_1}] \tag{B9}$$

Then we can get the two-stream general solution with surface albedo at arbitrary optical depth

$$I^+(\tau) = \frac{1}{2\pi}F\frac{[\omega_0 - \alpha(1-\bar{\mu}\rho)^2]e^{\rho(\tau_1-\tau)} - [\omega_0 - \alpha(1+\bar{\mu}\rho)^2]e^{-\rho(\tau_1-\tau)}}{[(1+\bar{\mu}\rho)^2 - \alpha\omega_0]e^{\rho\tau_1} - [(1-\bar{\mu}\rho)^2 - \alpha\omega_0]e^{-\rho\tau_1}} \tag{B10}$$

$$I^-(\tau) = \frac{1}{2\pi}F\frac{[(1+\bar{\mu}\rho)^2 - \alpha\omega_0]e^{\rho(\tau_1-\tau)} - [(1-\bar{\mu}\rho)^2 - \alpha\omega_0]e^{-\rho(\tau_1-\tau)}}{[(1+\bar{\mu}\rho)^2 - \alpha\omega_0]e^{\rho\tau_1} - [(1-\bar{\mu}\rho)^2 - \alpha\omega_0]e^{-\rho\tau_1}} \tag{B11}$$

At the top and bottom, emergent radiances are shown by equation (B13)-(B14).

$$I^+(0) = \frac{1}{2\pi}F\frac{[\omega_0 - \alpha(1-\bar{\mu}\rho)^2]e^{\rho\tau_1} - [\omega_0 - \alpha(1+\bar{\mu}\rho)^2]e^{-\rho\tau_1}}{[(1+\bar{\mu}\rho)^2 - \alpha\omega_0]e^{\rho\tau_1} - [(1-\bar{\mu}\rho)^2 - \alpha\omega_0]e^{-\rho\tau_1}} \tag{B13}$$

$$I^-(\tau_1) = \frac{2\bar{\mu}\rho F}{\pi}\frac{1}{[(1+\bar{\mu}\rho)^2 - \alpha\omega_0]e^{\rho\tau_1} - [(1-\bar{\mu}\rho)^2 - \alpha\omega_0]e^{-\rho\tau_1}} \tag{B14}$$

The non-dimensional value of reflectance is calculated in equation (B15).

$$R(\tau_1, \omega_0) = \frac{[\omega_0 - \alpha(1-\bar{\mu}\rho)^2]e^{\rho\tau_1} - [\omega_0 - \alpha(1+\bar{\mu}\rho)^2]e^{-\rho\tau_1}}{[(1+\bar{\mu}\rho)^2 - \alpha\omega_0]e^{\rho\tau_1} - [(1-\bar{\mu}\rho)^2 - \alpha\omega_0]e^{-\rho\tau_1}} \tag{B15}$$

2. One-line spectra

[33] Only pressure broadening is considered in this model as Doppler and natural broadenings are weak in the troposphere where most of the absorption occurs [*Goody*

609 *and Yung*, 1989]. The atmosphere is divided into two layers: a free troposphere with
610 absorption only and a PBL with absorption and scattering. We define the pressure at
611 the top of PBL to be P_1. In this model P_1 is defined to be 800 hPa, which is consistent
612 with the pressure level of CLARS instrument at the altitude of 1.7 km.

613 [34] The absorption coefficient of a Lorentzian absorption line shape is

614 $$k = S\frac{\alpha_L}{\pi}\frac{1}{{\alpha_L}^2 + (\nu - \nu_0)^2} \tag{B16}$$

615 where $\alpha_L = \alpha_L^0(p/p_0)$ is half-width of the line at the half-maximum [*Liou*, 2002],
616 p is the pressure and α_L^0 is the line width at the reference pressure p_0. The optical depth
617 of the free troposphere is given by

618 $$\tau_1 = \tau_{1a} = \frac{S\chi}{\pi mg}\int_0^{P_1}\frac{Ap}{(Ap)^2 + (\upsilon - \upsilon_0)^2}dp = \frac{S\chi}{2\pi mgA}\ln\frac{P_1^2 + [(\upsilon - \upsilon_0)/A]^2}{[(\upsilon - \upsilon_0)/A]^2} \tag{B17}$$

619 where S is the line strength constant, $A = \alpha_L / p = \alpha_L^0 / p_0$. The two constants A and
620 S can be obtained from the HITRAN database [*Rothman et al.*, 2008]. In this model,
621 for the CO_2 absorption line ν_0 = 6243.9 cm^{-1}, S = 1.52×10^{-23} cm, A = 7.2×10^{-7}
622 $cm^{-1}Pa^{-1}$; for the O_2 absorption line ν_0 = 7863.4 cm^{-1}, S = 4.78×10^{-26} cm, A =
623 5.5×10^{-7} $cm^{-1}Pa^{-1}$. χ is the volume mixing ratio of the absorbing gas (CO_2 and O_2).
624 We set χ to be 400 ppm for CO_2 and 0.21 for O_2. In the equation m = 4.8×10^{-26} kg is
625 the mean molecular weight of air, g is 9.8 m/s^2. Note that mg = 4.7×10^{-21} cm^2Pa is a
626 constant. Transmittance of the free troposphere is

627 $$T_1 = e^{-\tau_1} \tag{B18}$$

628 In the PBL, the total optical depth is

629 $$\tau_{2a} = \frac{S\chi}{\pi mg}\int_{P_1}^{P_s}\frac{Ap}{(Ap)^2 + (\upsilon - \upsilon_0)^2}dp = \frac{S\chi}{2\pi mgA}\ln\frac{P_s^2 + [(\upsilon - \upsilon_0)/A]^2}{P_1^2 + [(\upsilon - \upsilon_0)/A]^2} \tag{B19}$$

630 $$\tau_2 = \tau_{2a} + \tau_s \quad \text{(B20)}$$

631 $$\gamma = \frac{\tau_s}{\tau_{2a} + \tau_s} = \frac{\tau_s}{\tau_2} \quad \text{(B21)}$$

632 where P_s = 1030 hPa is the surface pressure. According to equation B(17), at the
633 center of the absorption line where $\nu = \nu_0$, we have a singular point with infinite
634 absorption optical depth. In the retrieval, most of the channels are away from the
635 singular point ($|\nu-\nu_0| > 0.001\text{cm}^{-1}$) where Lorentzian line shape is still a good
636 approximation. This problem can be avoided in our numerical model where we have
637 more realistic line shapes. The parameter γ is defined to be the ratio of AOD in the
638 PBL to the total optical depth in this layer. We can modify the radiative transfer
639 equation as

640 $$\mu \frac{dI(\tau,\mu)}{d\tau} = I(\tau,\mu) - \frac{1}{2}\omega_0 \gamma \int_{-1}^{1} I(\tau,\mu) d\mu \quad \text{(B22)}$$

641 [35] Repeating the calculations of the two-stream approximation, we can get the
642 reflectance of the PBL as equation (B23).

643 $$R_2 = \frac{[\omega_0\gamma - \alpha(1-\bar{\mu}\rho)^2]e^{\rho\tau_2} - [\omega_0\gamma - \alpha(1+\bar{\mu}\rho)^2]e^{-\rho\tau_2}}{[(1+\bar{\mu}\rho)^2 - \alpha\omega_0\gamma]e^{\rho\tau_2} - [(1-\bar{\mu}\rho)^2 - \alpha\omega_0\gamma]e^{-\rho\tau_2}} \quad \text{(B23)}$$

644 Finally, what we observe as the reflectance at the top of the PBL is

645 $$R = T_1 \cdot R_2 = e^{-\tau_1} \cdot \frac{[\omega_0\gamma - \alpha(1-\bar{\mu}\rho)^2]e^{\rho\tau_2} - [\omega_0\gamma - \alpha(1+\bar{\mu}\rho)^2]e^{-\rho\tau_2}}{[(1+\bar{\mu}\rho)^2 - \alpha\omega_0\gamma]e^{\rho\tau_2} - [(1-\bar{\mu}\rho)^2 - \alpha\omega_0\gamma]e^{-\rho\tau_2}} \quad \text{(B24)}$$

646 where τ_1, τ_2 and γ are wavelength dependent. To incorporate the variation of solar
647 zenith angle θ, we assume in each layer the optical depth

648 $$\tau_i(\theta) = \frac{\tau_i(0)}{\cos(\theta)} \quad \text{(B25)}$$

649

650 **References:**

651 Ackermann, I. J., H. Hass, M. Memmesheimer, A. Ebel, F. S. Binkowski, and U.
652 Shankar (1998), Modal aerosol dynamics model for Europe: Development and
653 first applications, *Atmos Environ*, *32*(17), 2981-2999,
654 doi: 10.1016/S1352-2310(98)00006-5.

655 Andrews, E., et al. (2006), Comparison of methods for deriving aerosol asymmetry
656 parameter, *J Geophys Res-Atmos*, *111*(D5), doi: 10.1029/2004jd005734.

657 Basu, S., et al. (2013), Global CO_2 fluxes estimated from GOSAT retrievals of total
658 column CO_2, *Atmos Chem Phys*, *13*(17), 8695-8717, doi:
659 10.5194/acp-13-8695-2013.

660 Belton, M. J. S., D. M. Hunten, R. M. Goody (1968), Quantitative Spectroscopy of
661 Venusin the Region 8,000 -11,000 A, in *The Atmospheres of Venus and Mars*,
662 edited, New York: Gordon & Breach.

663 Boucher, O. (1998), On aerosol direct shortwave forcing and the Henyey-Greenstein
664 phase function, *J Atmos Sci*, *55*(1), 128-134,
665 doi: 10.1175/1520-0469(1998)055%3C0128:OADSFA%3E2.0.CO;2

666 Bovensmann, H., J. P. Burrows, M. Buchwitz, J. Frerick, S. Noel, V. V. Rozanov, K.
667 V. Chance, and A. P. H. Goede (1999), SCIAMACHY: Mission objectives and
668 measurement modes, *J Atmos Sci*, *56*(2), 127-150,
669 doi: 10.1175/1520-0469(1999)056<0127:SMOAMM>2.0.CO;2.

670 Butz, A., et al. (2011), Toward accurate CO_2 and CH_4 observations from GOSAT,
671 *Geophys Res Lett*, *38*, doi: 10.1029/2011gl047888.

672 Chamberlain, J. W. (1970), Behavior of Absorption Lines in a Hazy Planetary
673 Atmosphere, *Astrophys J*, *159*(1p1), 137-158, doi: 10.1086/150297.
674 Collins, D. R., H. H. Jonsson, H. Liao, R. C. Flagan, J. H. Seinfeld, K. J. Noone, and
675 S. V. Hering (2000), Airborne analysis of the Los Angeles aerosol, *Atmos*
676 *Environ*, *34*(24), 4155-4173, doi: 10.1016/S1352-2310(00)00225-9.
677 Crisp, D., et al. (2004), The orbiting carbon observatory (OCO) mission, *Adv Space*
678 *Res-Series*, *34*(4), 700-709, doi: 10.1016/j.asr.2003.08.062.
679 Crisp, D., et al. (2012), The ACOS CO_2 retrieval algorithm - Part II: Global X_{CO2}
680 data characterization, *Atmos Meas Tech*, *5*(4), 687-707, doi:
681 10.5194/amt-5-687-2012.
682 Derooij, W. A., and C. C. A. H. Vanderstap (1984), Expansion of Mie Scattering
683 Matrices in Generalized Spherical-Functions, *Astron Astrophys*, *131*(2),
684 237-248.
685 Dudhia, A., P. E. Morris, and R. J. Wells (2002), Fast monochromatic radiative
686 transfer calculations for limb sounding, *J Quant Spectrosc Ra*, *74*(6), 745-756,
687 doi: 10.1016/S0022-4073(01)00285-0.
688 Duren, R. M., and C. E. Miller (2012), Measuring the carbon emissions of
689 megacities, *Nat Clim Change*, *2*(8), 560-562, doi:10.1038/nclimate1629
690 Fu, D., T. J. Pongetti, J.-F. L. Blavier, T. J. Crawford, K. S. Manatt, G. C. Toon, K. W.
691 Wong, and S. P. Sander (2013), Near-infrared remote sensing of Los Angeles
692 trace gas distributions from a mountaintop site, *Atmos Meas Tech Discuss*, *6*,
693 8807–8854, doi:10.5194/amtd-6-8807-2013.

694 Funk, O., and K. Pfeilsticker (2003), Photon path length distributions for cloudy
695 skies - oxygen A-band measurements and model calculations, *Ann*
696 *Geophys-Germany*, *21*(3), 615-626, doi: 10.5194/angeo-21-615-2003
697 Goody, R. M., and Y. L. Yung (1989), *Atmospheric Radiation: Theoretical Basis*,
698 *Second Edition*, Oxford University Press.
699 Hansen, J. E., and L. D. Travis (1974), Light-Scattering in Planetary Atmospheres,
700 *Space Sci Rev*, *16*(4), 527-610, doi: 10.1007/Bf00168069.
701 Haywood, J. M., and K. P. Shine (1995), The Effect of Anthropogenic Sulfate and
702 Soot Aerosol on the Clear-Sky Planetary Radiation Budget, *Geophys Res Lett*,
703 *22*(5), 603-606, doi: 10.1029/95gl00075.
704 Henyey, L. G., and J. L. Greenstein (1941), Diffuse radiation in the galaxy,
705 *Astrophys J*, *93*(1), 70-83, doi: 10.1086/144246.
706 Hersey, S. P., et al. (2013), Composition and hygroscopicity of the Los Angeles
707 Aerosol: CalNex, *J Geophys Res-Atmos*, *118*(7), 3016-3036, doi:
708 10.1002/Jgrd.50307.
709 Hersey, S. P., J. S. Craven, K. A. Schilling, A. R. Metcalf, A. Sorooshian, M. N.
710 Chan, R. C. Flagan, and J. H. Seinfeld (2011), The Pasadena Aerosol
711 Characterization Observatory (PACO): chemical and physical analysis of the
712 Western Los Angeles basin aerosol, *Atmos Chem Phys*, *11*(15), 7417-7443, doi:
713 10.5194/acp-11-7417-2011.
714 Hess, M., P. Koepke, and I. Schult (1998), Optical properties of aerosols and clouds:
715 The software package OPAC, *B Am Meteorol Soc*, *79*(5), 831-844,

716 doi: 10.1175/1520-0477(1998)079<0831:Opoaac>2.0.Co;2.
717 Holben, B. N., et al. (1998), AERONET - A federated instrument network and data
718 archive for aerosol characterization, *Remote Sens Environ*, *66*(1), 1-16, doi:
719 10.1016/S0034-4257(98)00031-5.
720 Holben, B. N., et al. (2001), An emerging ground-based aerosol climatology: Aerosol
721 optical depth from AERONET, *J Geophys Res-Atmos*, *106*(D11), 12067-12097,
722 doi: 10.1029/2001jd900014.
723 Houweling, S., W. Hartmann, I. Aben, H. Schrijver, J. Skidmore, G. J. Roelofs, and F.
724 M. Breon (2005), Evidence of systematic errors in SCIAMACHY-observed CO_2
725 due to aerosols, *Atmos Chem Phys*, 5, 3003-3013, doi:
726 10.5194/acp-5-3003-2005.
727 IPCC (2013), *Climate Change, the Fifth Assessment Report (AR5) of the United*
728 *Nations Intergovernmental Panel on Climate Change*, Intergovernmental Panel
729 on Climate Change.
730 Kahn, R. A., B. J. Gaitley, J. V. Martonchik, D. J. Diner, K. A. Crean, and B. Holben
731 (2005), Multiangle Imaging Spectroradiometer (MISR) global aerosol optical
732 depth validation based on 2 years of coincident Aerosol Robotic Network
733 (AERONET) observations, *J Geophys Res-Atmos*, *110*(D10), doi:
734 10.1029/2004jd004706.
735 Kalnay, E., et al. (1996), The NCEP/NCAR 40-year reanalysis project, *B Am*
736 *Meteorol Soc*, *77*(3), 437-471,
737 doi: 10.1175/1520-0477(1996)077<0437:Tnyrp>2.0.Co;2.

738 Kort, E. A., C. Frankenberg, C. E. Miller, and T. Oda (2012), Space-based
739 observations of megacity carbon dioxide, *Geophys Res Lett*, *39*, doi:
740 10.1029/2012gl052738.
741 Kryzhevoi, N. V., G. V. Efimov, and R. Wehrse (2001), Analytic solution of the
742 radiative transfer equation in the two-stream approximation, *Astron Astrophys*,
743 *370*(2), 707-714, doi: 10.1051/0004-6361:20010310
744 Kuang, Z. M., J. Margolis, G. Toon, D. Crisp, and Y. Yung (2002), Spaceborne
745 measurements of atmospheric CO_2 by high-resolution NIR spectrometry of
746 reflected sunlight: An introductory study, *Geophys Res Lett*, *29*(15), doi:
747 10.1029/2001gl014298.
748 Kylling, A., K. Stamnes, and S. C. Tsay (1995), A Reliable and Efficient 2-Stream
749 Algorithm for Spherical Radiative-Transfer - Documentation of Accuracy in
750 Realistic Layered Media, *J Atmos Chem*, *21*(2), 115-150, doi:
751 10.1007/Bf00696577.
752 Liou, K. N. (1974), Analytic 2-Stream and 4-Stream Solutions for Radiative-Transfer,
753 *J Atmos Sci*, *31*(5), 1473-1475,
754 doi: 10.1175/1520-0469(1974)031<1473:Atsafs>2.0.Co;2.
755 Liou, K. N. (2002), *An Introduction to Atmospheric Radiation, Second Edition*,
756 Academic Press.
757 Meador, W. E., and W. R. Weaver (1980), 2-Stream Approximations to
758 Radiative-Transfer in Planetary-Atmospheres - a Unified Description of Existing
759 Methods and a New Improvement, *J Atmos Sci*, *37*(3), 630-643, doi:

760 10.1175/1520-0469(1980)037<0630:Tsatrt>2.0.Co;2.
761 Natraj, V., R. L. Shia, and Y. L. Yung (2010), On the use of principal component
762 analysis to speed up radiative transfer calculations, *J Quant Spectrosc Ra*, *111*(5),
763 810-816, doi: 10.1016/j.jqsrt.2009.11.004.
764 Oshchepkov, S., et al. (2012), Effects of atmospheric light scattering on
765 spectroscopic observations of greenhouse gases from space: Validation of
766 PPDF-based CO_2 retrievals from GOSAT, *J Geophys Res-Atmos*, *117*, doi:
767 10.1029/2012jd017505.
768 Rodgers, C. D. (2000), *Inverse Methods for Atmospheric Sounding: Theory and*
769 *Practice*, World Scientific Publisbing Co. Pte. Ltd.
770 Rothman, L. S., et al. (2009), The HITRAN 2008 molecular spectroscopic database,
771 *J Quant Spectrosc Ra*, *110*(9-10), 533-572, doi: 10.1016/j.jqsrt.2009.02.013.
772 Schell, B., I. J. Ackermann, H. Hass, F. S. Binkowski, and A. Ebel (2001), Modeling
773 the formation of secondary organic aerosol within a comprehensive air quality
774 model system, *J Geophys Res-Atmos*, *106*(D22), 28275-28293, doi:
775 10.1029/2001jd000384.
776 Seidel, F. C., and C. Popp (2012), Critical surface albedo and its implications to
777 aerosol remote sensing, *Atmos Meas Tech*, *5*(7), 1653-1665, doi:
778 10.5194/amt-5-1653-2012.
779 Seinfeld, J. H., and S. N. Pandis (2006), *Atmospheric Chemistry and Physics: From*
780 *Air Pollution to Climate Change, Second Edition*, John Wiley & Sons, Inc.
781 Skamarock, W. C., J. B. Klemp, J. Dudhia, D. O. Gill, D. M. Barker, W. Wang, and J.

782 G. Powers (2005), A description of the advanced research WRF version 2.
783 NCAR Tech. Note NCAR/TN-468+STR, 8 pp.
784 Spurr, R., and V. Natraj (2011), A linearized two-stream radiative transfer code for
785 fast approximation of multiple-scatter fields, *J Quant Spectrosc Ra*, *112*(16),
786 2630-2637, doi: 10.1016/j.jqsrt.2011.06.014.
787 Spurr, R. J. D. (2006), VLIDORT: A linearized pseudo-spherical vector discrete
788 ordinate radiative transfer code for forward model and retrieval studies in
789 multilayer multiple scattering media, *J Quant Spectrosc Ra*, *102*(2), 316-342,
790 doi: 10.1016/j.jqsrt.2006.05.005.
791 Takemura, T., T. Nakajima, O. Dubovik, B. N. Holben, and S. Kinne (2002),
792 Single-scattering albedo and radiative forcing of various aerosol species with a
793 global three-dimensional model, *J Climate*, *15*(4), 333-352,
794 doi: 10.1175/1520-0442(2002)015<0333:Ssaarf>2.0.Co;2.
795 Wiscombe, W. J. (1977), Delta-M Method - Rapid yet Accurate Radiative Flux
796 Calculations for Strongly Asymmetric Phase Functions, *J Atmos Sci*, *34*(9),
797 1408-1422, doi: 10.1175/1520-0469(1977)034<1408:Tdmrya>2.0.Co;2.
798 Yokota, T., Y. Yoshida, N. Eguchi, Y. Ota, T. Tanaka, H. Watanabe, and S.
799 Maksyutov (2009), Global Concentrations of CO_2 and CH_4 Retrieved from
800 GOSAT: First Preliminary Results, *Sola*, *5*, 160-163, doi:
801 10.2151/sola.2009-041.
802 Yoshida, Y., Y. Ota, N. Eguchi, N. Kikuchi, K. Nobuta, H. Tran, I. Morino, and T.
803 Yokota (2011), Retrieval algorithm for CO_2 and CH_4 column abundances from

short-wavelength infrared spectral observations by the Greenhouse gases observing satellite, *Atmos Meas Tech*, *4*(4), 717-734, doi: 10.5194/amt-4-717-2011.

826 **Table captions:**

827

828 **Table 1**. Model configurations for retrieval.

829

830 **Table 2.** Aerosol composition and optical properties in the LA region.

831

832

833

834

835

836

837

838

839

840

841

842

843

844

845

846

847

Table 1. Model configurations for retrieval.

	model	α	SSA	g	phase function
Case A	analytic	0.1	0.99	0	isotropic
Case B	numerical	0.23	0.99	0	isotropic
Case C	numerical	0.23	0 ~ 0.99	0 ~ 1	Henyey-Greenstein
Case D	numerical	0.23	realistic	realistic	realistic

Table 2. Aerosol composition and optical properties in the LA region.

	Organic	Seasalt (accum)	Seasalt (coarse)	Soot	Sulfate
percentage	4.9%	31.7%	38.1%	7.9%	17.4%
SSA	0.872	0.998	0.985	0.040	0.999
g	0.55	0.79	0.82	0.15	0.69

[*Ackermann et al.*, 1998; *Schell et al.*, 2001]

Figure captions:

Figure 1. Schematic figure of CLARS measurement geometries.

Figure 2. Variations of CLARS measured SCD v.s. geometric SCD from the morning to the afternoon, for (a) CO_2 and (b) O_2. A, B and C indicate morning, noon and afternoon. Units for CO_2 and O_2 SCDs are scaled by 10^{22} and 10^{25} molecule/cm^2, respectively. The red lines indicate 1:1 correspondence between measured and geometric SCDs.

Figure 3. Spectra of the O_2 absorption band with different AOD in the PBL. (a) Absolute radiance from the numerical model. In the model surface albedo is 0.23, SSA is 0.99 and g is 0. The absolute radiance assumes that the radiance at the top of atmosphere is equal to 1. (b) Normalized radiance from the numerical model (c) Measurements of normalized radiance from CLARS instrument on 13 March 2013 (clear) and 23 March 2013 (hazy) at 4:30 pm.

Figure 4. One-line spectra simulated by the analytic model for a CO_2 absorption line. (a) Absolute reflectance with different AOD and ω_0 in the PBL. (b) Normalized reflectance with different AOD in the PBL, ω_0=0.99. (c) Normalized reflectance with different AOD in the PBL, ω_0=0.2. (d) Normalized reflectance with different CO_2 concentrations, AOD = 0. The central wavenumber ν_0 = 6243.9 cm^{-1} has been

subtracted.

Figure 5. Retrieval of CO_2 concentrations in the free troposphere and the PBL with increasing AOD. The red lines indicate retrievals with SZA = 60^o. The blue lines indicate retrievals with SZA = 0^o. The solid lines indicate retrievals in the free troposphere and the dashed lines indicate retrievals in the PBL.

Figure 6. Simulated 'U shape' of the SCD daily variations, assuming AOD increases linearly from 0 to 0.1 in the PBL and SZA varies linearly from -60^o to 60^o for absorption lines of (a) CO_2 with ω_0=0.99 (b) CO_2 with ω_0=0.2 (c) O_2 with ω_0=0.99 (d) O_2 with ω_0=0.2. Units for CO_2 and O_2 SCDs are scaled as in Figure 2. The red lines indicate 1:1 correspondence between measured and geometric SCDs.

Figure 7. Simulated spectra of (a) CO_2 absorption band 6220-6245 cm^{-1} (b) O_2 absorption band 7910-7935 cm^{-1}.

Figure 8. Retrieval of (a) CO_2 concentrations in the free troposphere and the PBL with increasing AOD (b) O_2 concentrations and (c) X_{CO_2}. The Black dotted lines show the true or the *a priori* values. The red star corresponds to the left-bottom corner in Figure 9(c).

Figure 9. Retrieval biases caused by different kinds of aerosols in the SSA-g

parameter space with AOD = 0.1 for (a) CO_2 SCD (b) O_2 SCD and (c) X_{CO_2}. SCD biases are displayed in percentage with respect to the value with AOD = 0. The true value of X_{CO_2} with AOD = 0 is 400.8 ppm. The bottom-left corner of panel (c) corresponds to the value marked with a red star '*' in Figure 8(c).

Figure 10. Comparison between the simulated and measured SCD daily variations on 23 March 2013 in West Pasadena for (a) CO_2 SCD and (b) O_2 SCD. Units for the CO_2 and O_2 SCDs are scaled as in Figure 2. The red lines indicate 1:1 correspondence between measured and geometric SCDs.

927 **Figure 1.**

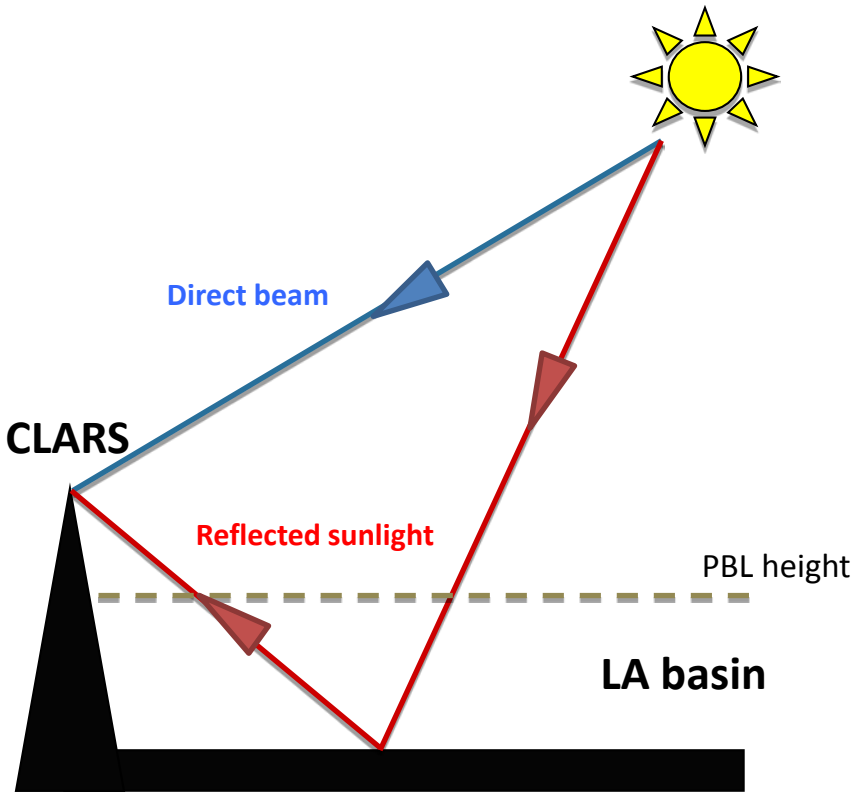

928

929 **Figure 1**. Schematic figure of CLARS measurement geometries.

930

931

932

933

934

935

936

937

938

939

940 **Fig**

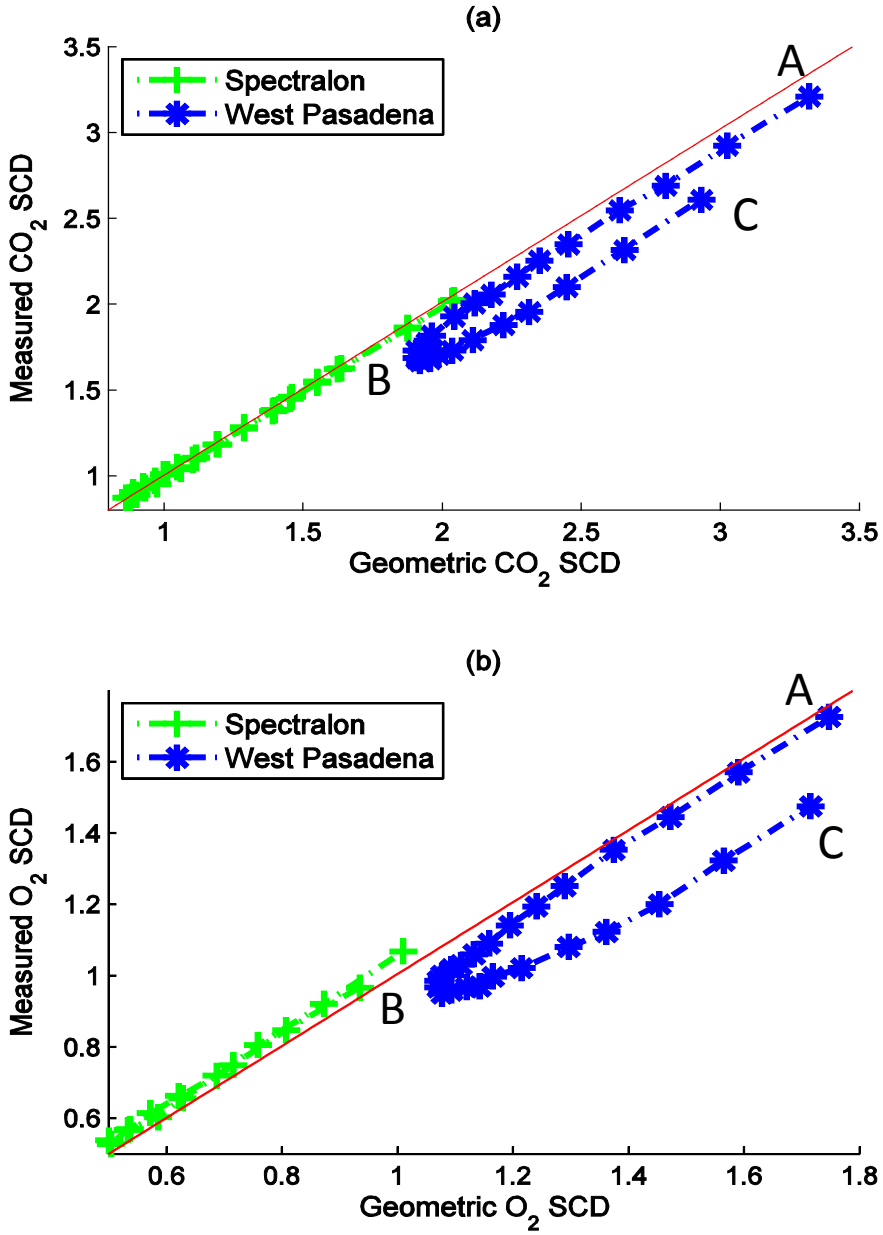

941

942 **Figure 2.** Variations of CLARS measured SCD v.s. geometric SCD from the
943 morning to the afternoon, for (a) CO_2 and (b) O_2. A, B and C indicate morning, noon
944 and afternoon. Units for CO_2 and O_2 SCDs are scaled by 10^{22} and 10^{25} molecule/cm^2,
945 respectively. The red lines indicate 1:1 correspondence between measured and
946 geometric SCDs.

Figure 3.

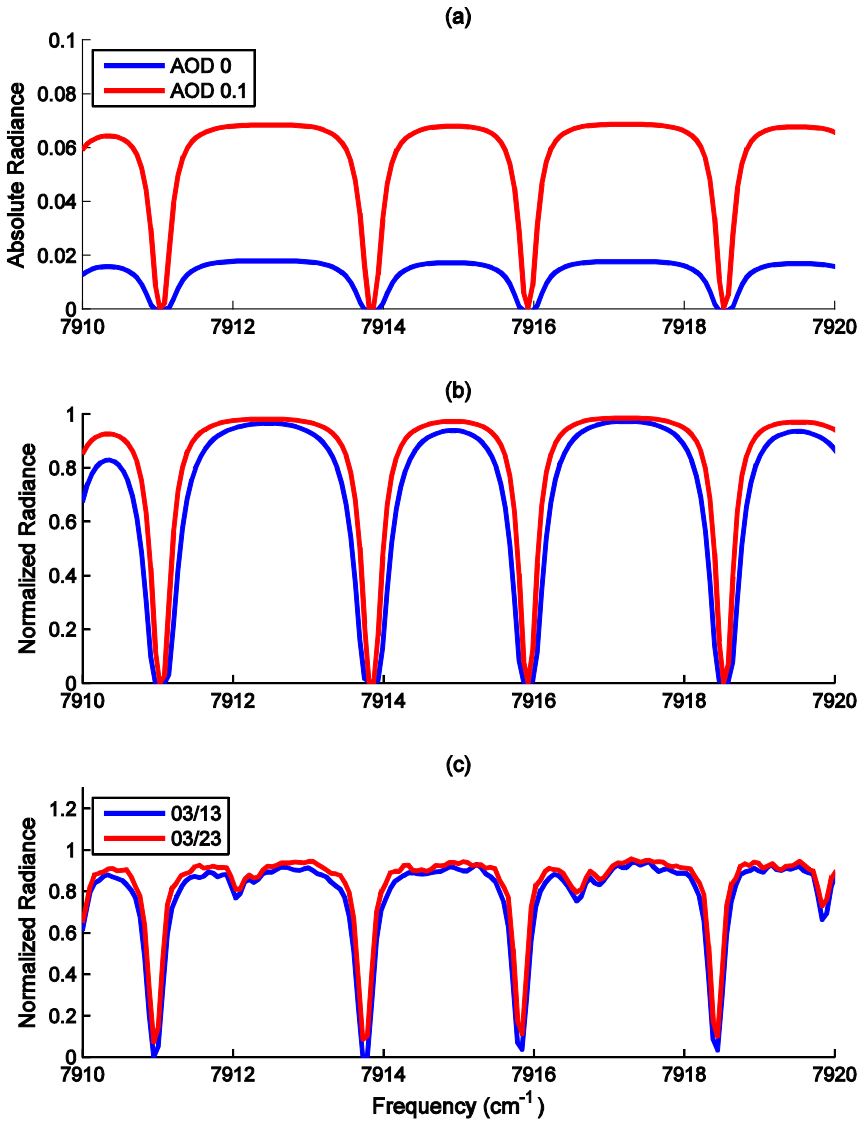

Figure 3. Spectra of the O_2 absorption band with different AOD in the PBL. (a) Absolute radiance from the numerical model. In the model surface albedo is 0.23, SSA is 0.99 and g is 0. The absolute radiance assumes that the radiance at the top of atmosphere is equal to 1. (b) Normalized radiance from the numerical model (c) Measurements of normalized radiance from CLARS instrument on 13 March 2013 (clear) and 23 March 2013 (hazy) at 4:30 pm.

955 **Figure 4.**

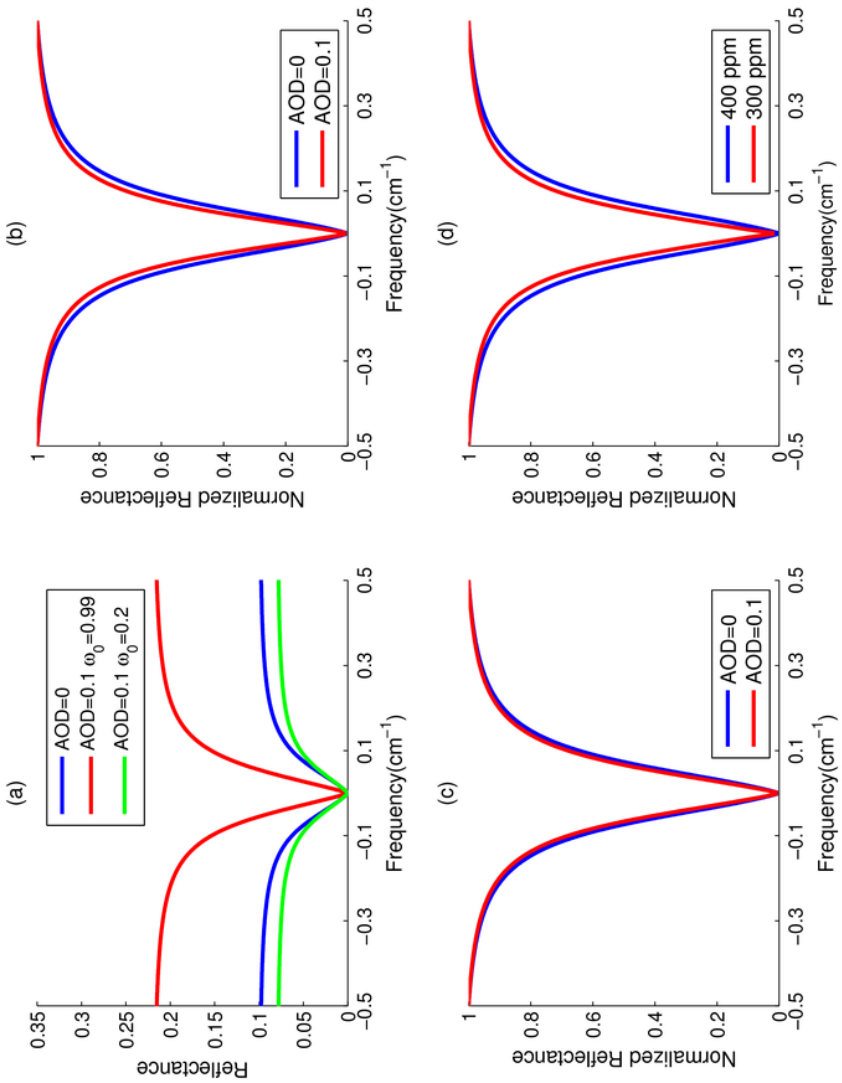

956

957 **Figure 4.** One-line spectra simulated by the analytic model for a CO_2 absorption line.

958 (a) Absolute reflectance with different AOD and ω_0 in the PBL. (b) Normalized

959 reflectance with different AOD in the PBL, ω_0=0.99. (c) Normalized reflectance with

960 different AOD in the PBL, ω_0=0.2. (d) Normalized reflectance with different CO_2

961 concentrations, AOD = 0. The central wavenumber ν_0 = 6243.9 cm^{-1} has been

962 subtracted.

Figure 5.

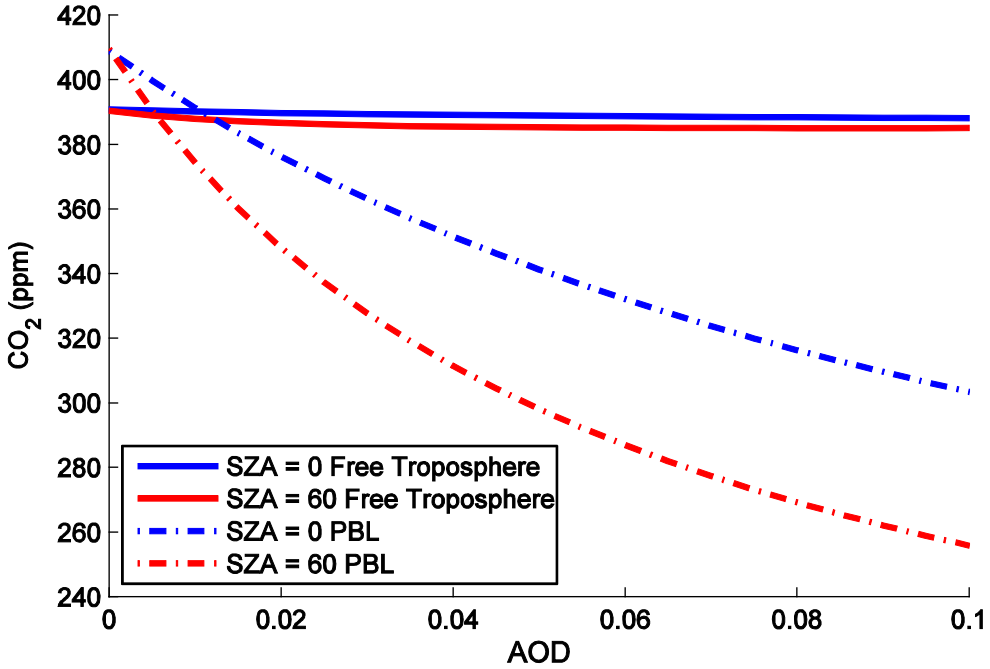

Figure 5. Retrieval of CO_2 concentrations in the free troposphere and the PBL with increasing AOD. The red lines indicate retrievals with SZA = 60^o. The blue lines indicate retrievals with SZA = 0^o. The solid lines indicate retrievals in the free troposphere and the dashed lines indicate retrievals in the PBL.

977 **Figure 6.**

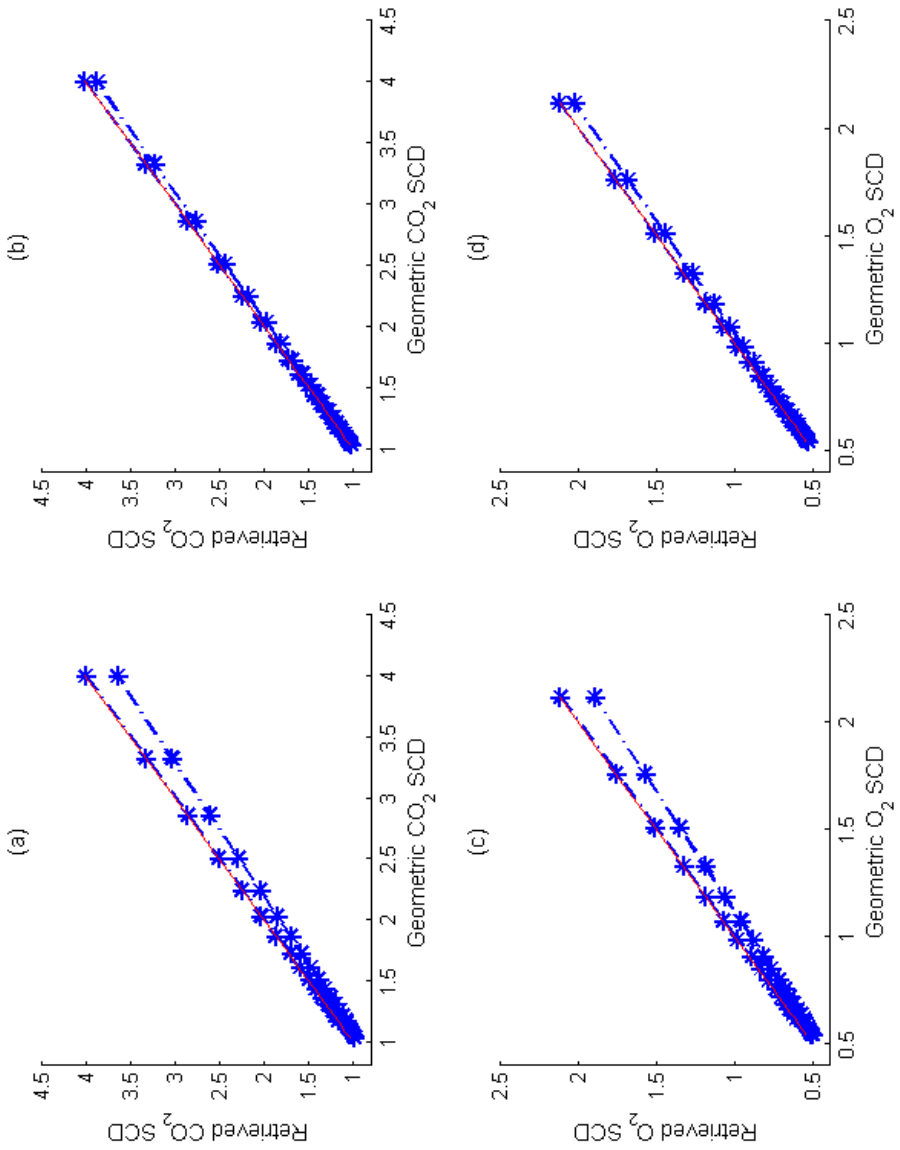

978

979 **Figure 6.** Simulated 'U shape' of the SCD daily variations, assuming AOD increases
980 linearly from 0 to 0.1 in the PBL and SZA varies linearly from -60^o to 60^o for
981 absorption lines of (a) CO_2 with ω_0=0.99 (b) CO_2 with ω_0=0.2 (c) O_2 with ω_0=0.99 (d)
982 O_2 with ω_0=0.2. Units for CO_2 and O_2 SCDs are scaled as in Figure 2. The red lines
983 indicate 1:1 correspondence between measured and geometric SCDs.

Figure 7.

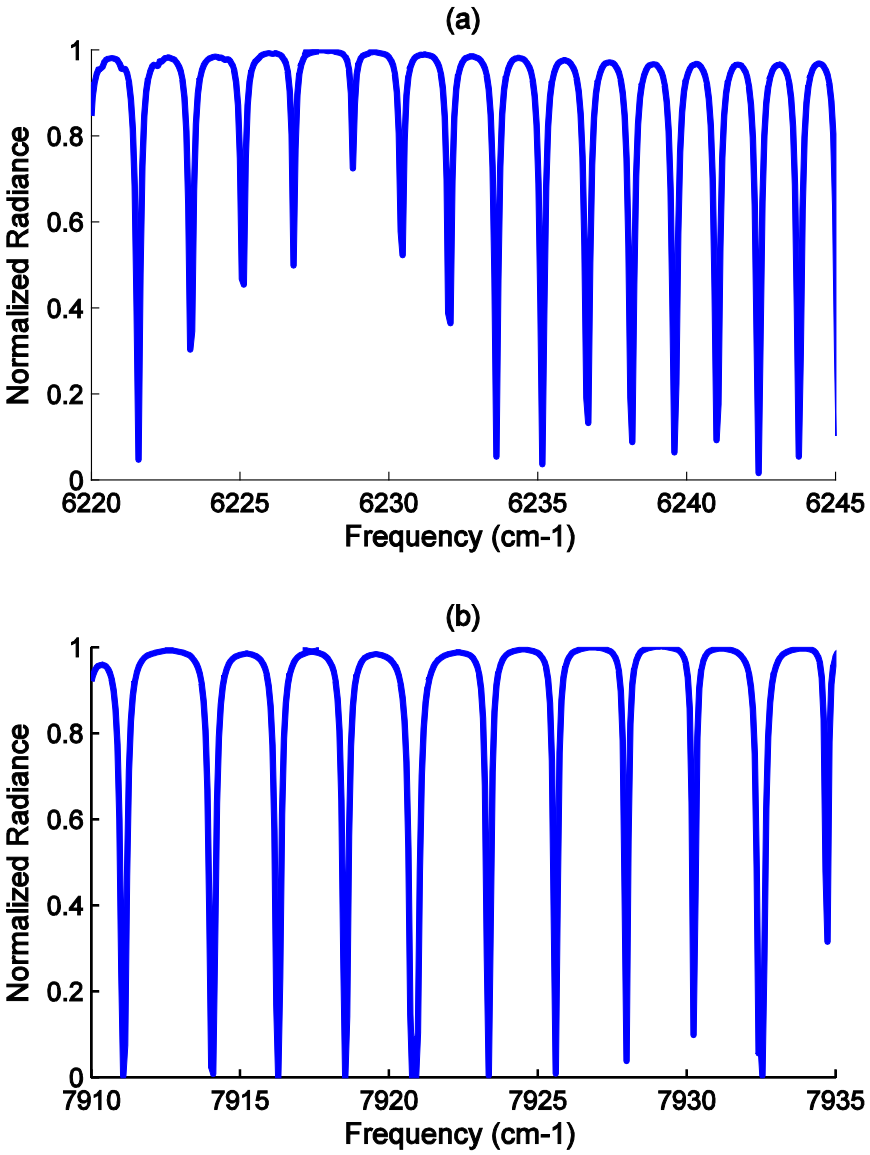

Figure 7. Simulated spectra of (a) CO_2 absorption band 6220-6245 cm^{-1} (b) O_2 absorption band 7910-7935 cm^{-1}.

992 **Figure 8.**

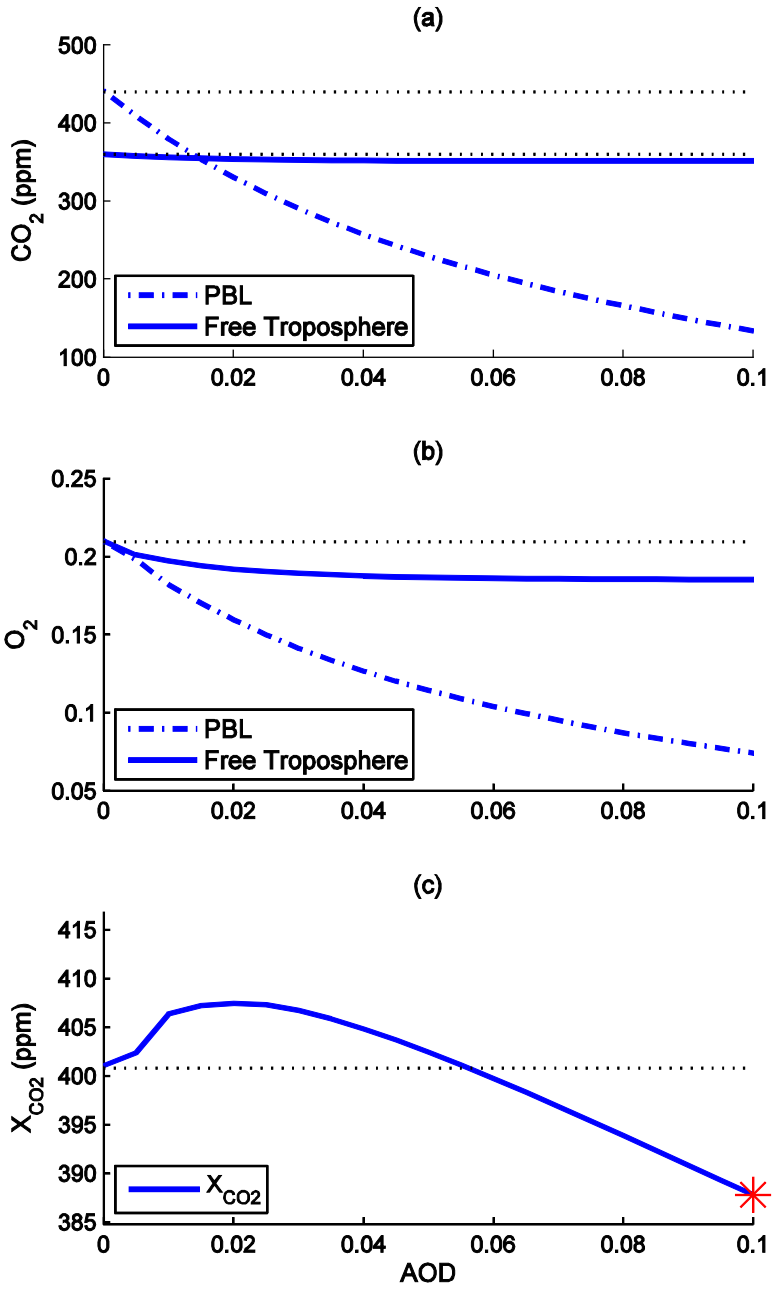

993

994 **Figure 8.** Retrieval of (a) CO_2 concentrations in the free troposphere and the PBL

995 with increasing AOD (b) O_2 concentrations and (c) X_{CO_2}. The Black dotted lines

996 show the true or the *a priori* values. The red star corresponds to the left-bottom

997 corner in Figure 9(c).

Figure 9.

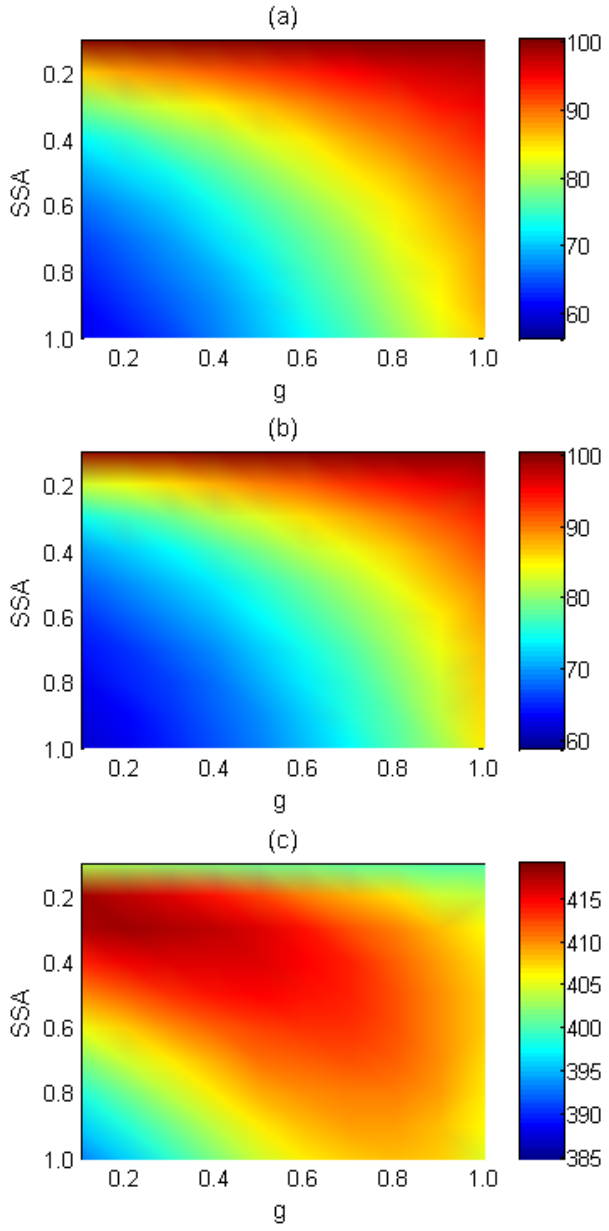

Figure 9. Retrieval biases caused by different kinds of aerosols in the SSA-g parameter space with AOD = 0.1 for (a) CO_2 SCD (b) O_2 SCD and (c) X_{CO_2}. SCD biases are displayed in percentage with respect to the value with AOD = 0. The true value of X_{CO_2} with AOD = 0 is 400.8 ppm. The bottom-left corner of panel (c) corresponds to the value marked with a red star '*' in Figure 8(c).

1005 **Figure 10.**

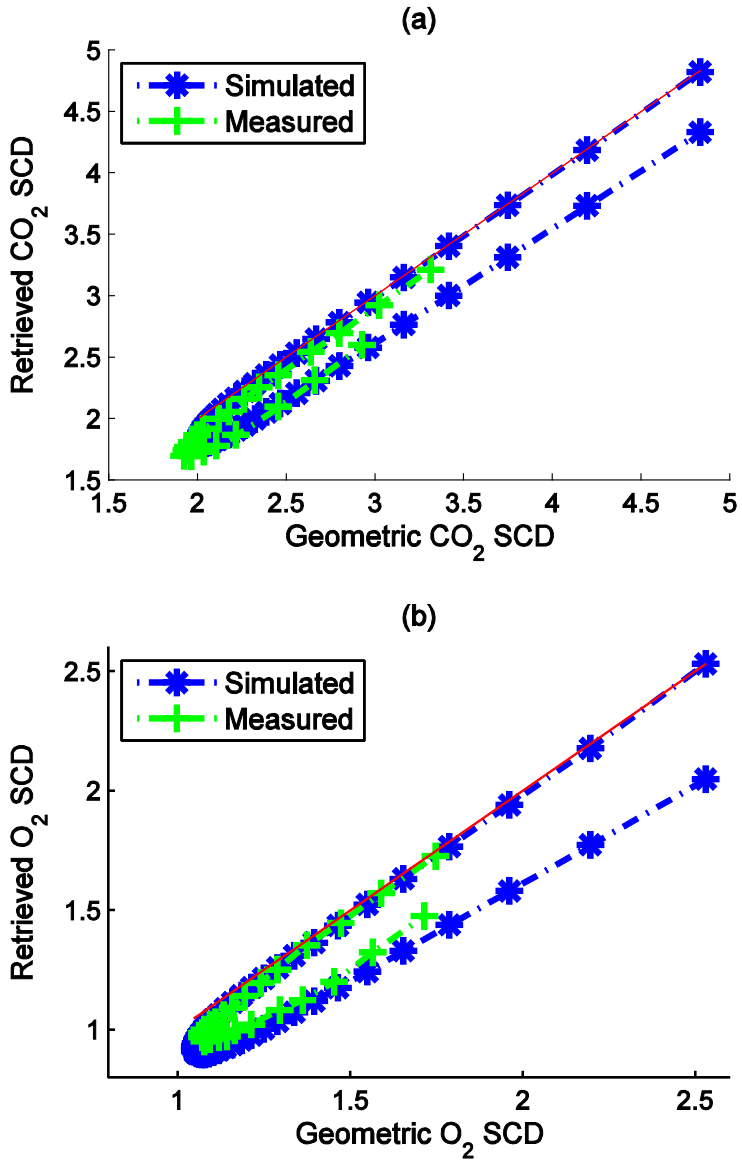

1006

1007 **Figure 10.** Comparison between the simulated and measured SCD daily variations

1008 on 23 March 2013 in West Pasadena for (a) CO_2 SCD and (b) O_2 SCD. Units for the

1009 CO_2 and O_2 SCDs are scaled as in Figure 2. The red lines indicate 1:1

1010 correspondence between measured and geometric SCDs.

1011